Formation mechanism of radial and circular cracks promoted by delamination in drying silica colloidal deposits

Xujing Liu [1,*] Mengqi Liu [1,*] Yi Sun,[1] Senjiang Yu [2,†] and Yong Ni [1,‡]

[1]*CAS Key Laboratory of Mechanical Behavior and Design of Materials, Department of Modern Mechanics, University of Science and Technology of China, Hefei, Anhui 230026, People's Republic of China*

[2]*Key Laboratory of Novel Materials for Sensor of Zhejiang Province, College of Materials and Environmental Engineering, Hangzhou Dianzi University, Hangzhou 310018, People's Republic of China*

(Received 3 February 2024; accepted 6 August 2024; published 5 September 2024)

Cracks with radial and circular patterns are appealing in nature and industry. Although morphologies and propagation conditions of cracks are extensively studied, the formation mechanism of crack pattern by the interaction of channel fracture and interfacial delamination remains elusive. Here, we present the transition of radial to coexisting radial and circular crack patterns when the thickness of colloidal deposits on both hard and soft substrates exceeds a critical value, through the colloidal volume fraction dependence. In addition, a thickness-dependent phase diagram from radial crack to coexistence of radial and circular cracks was constructed with respect to the radius and the volume fractions of silica colloidal deposits. A phase-field fracture model is developed to elucidate how the formation of radial cracks is facilitated by simultaneous delamination. The warping-induced radial tensile stress at the bottom surface of the striped deposit is proportional to the thickness. It leads to subsequent nucleation and growth of circular cracks in thick deposits. This work provides insight into the formation mechanism of complex crack patterns in drying colloidal deposits and revolutionizes the design space of crack-based micro-nano structures.

DOI: 10.1103/PhysRevE.110.034801

I. INTRODUCTION

Controlling the evaporation of self-assembled suspension on substrates is a common method to obtain high-quality colloidal deposits [1–4]. However, this method is inevitably accompanied by complex cracking problems [5]. The nucleation and propagation of cracks are induced by residual tensile stresses that result from depositing processes, drying processes, thermal expansion mismatch, or mechanical loading [6–10]. The cracks may stop at the interface to form channel cracks or deflect into the interface to generate delamination, which depends on the material property of the film-substrate system [11]. Classic channel crack networks are extensively observed in china crockery, old paintings, and dry mud [12–14]. They propagate along a straight trajectory, deflecting only near the previous crack path, where they tend to connect perpendicularly to the free boundary. After the complete establishment of the previous fracture pattern, delamination may eventually occur [13]. Conversely, during the propagation of the crack, delamination may occur simultaneously and interact to change the propagation path when the film-substrate adhesion is relatively weak. The detailed interaction mode between the crack and delamination is based on the evaporation geometry, chemical property, and drying condition, which might achieve attractive crack morphologies [2,8,15–20]. These complex crack morphologies are attributed not only to the propagation of channel cracks but also to the coupling and propagation sequence of cracks and delamination [21,22]. Consequently, it is essential to understand the interaction of cracks and delamination in colloidal deposits.

The well-known drying crack patterns include polygon [12,17,23,24], linear [25], wavy [26], spiral [16,27], radial [3,7,28–31], and circular [18,32–34] structures. Among these, the radial and circular crack patterns have attracted substantial attention in both experimental observations and theoretical understandings [8,19,31–34]. It is believed that the formation of radial or circular cracks is influenced by modulus mismatch in film-substrate, preexisting flaws, and contact-line movement [35–38]. The substrate elasticity modulus determines the crack orientation by changing the in-plane stress distribution [35,36]. Circular cracks form on soft substrates, while radial cracks form on hard substrates. A preexisting track in the deposit is essential for initiating and propagating cracks along a circular path [37]. The movement of the contact line during drying influences stress development and relaxation in the deposit, which impacts crack formation and pattern [38]. The effect of material properties and environmental conditions on circular and radial cracks has been reasonably explored, but an exploration of the interplay of delamination and crack is scarce. When a drop of an aqueous suspension of silica nanoparticles is deposited onto a glass slide, the produced solid deposit may undergo interfacial delamination and radial cracking during drying [7]. In colloidal particle deposits, both the initiation of cracks and the onset of delamination are assumed to be governed by Griffith's criterion. The capillary

*These authors contributed equally to this work.
†Contact author: sjyu@hdu.edu.cn
‡Contact author: yni@ustc.edu.cn

 ©2024 American Physical Society

pressures within the system during the drying process contributes to the accumulation of elastic energy, which provides a driving force for the occurrence of crack nucleation or film delamination [28]. Delaminated deposits may exhibit warping due to the accumulation of stress and bending moment, resulting in the formation of regular petal-like structures [29]. The petals continue to grow towards the center of the drop and bend upwards [31]. However, these observations fail to capture the critical transition of radial to coexisting radial and circular crack and to elucidate why radial cracks are associated with interfacial delamination. The underlying formation mechanism requires further investigation.

In this work, we report the formation and evolution of radial cracks and coexisting circular and radial cracks coupled with interfacial delamination. The radial cracks nucleate at the edge and propagate accompanied by deposits delamination. When the deposit thickness exceeds a critical value, the circular cracks nucleate at the bottom of the deposits and propagate along the thickness direction. Additionally, a diagram is proposed to classify crack morphologies based on the deposit thickness. Furthermore, a phase-field fracture modeling is developed to simulate the propagation of cracks with or without delamination. The results elucidate that anisotropic stress release due to the delamination causes the crack to propagate radially. The nucleation and growth of circular cracks are attributed to the radial tensile stress induced by warping, which is proportional to the deposit thickness.

II. EXPERIMENTAL DETAILS

A. Desiccation experiment

The colloidal suspensions of silica nanoparticles ($\sim$15 nm diameter) were diluted into deionized water (Barnstead NanoPure) to obtain various concentrations. Here, the diluted suspensions with volume fractions ϕ of 0.5, 1, 5, 10, 15, 20, 25, and 30% were used in our experiment. Glass slides were utilized as supporting substrates, which were initially cleaned with acetone, alcohol, and deionized water before being dried with a stream of nitrogen. The prepared colloidal suspensions were dropped onto the cleaned glass substrates using a micropipette, with a droplet volume (V) of 1 μL and a droplet area radius (R) of $\sim$1 mm. The droplets were allowed to evaporate naturally at ambient temperature and pressure.

B. Characterization

A reflective optical microscope (Olympus, BX51) and a camera connected to a computer via the connectors and software were used to observe and capture the drying processes from vertical and horizontal perspectives, respectively. The top and side views of the droplets during drying were extracted from the recorded videos. Subsequently, the corresponding characteristic parameters of the drying droplets were measured based on the extracted micrographs. After complete evaporation, the height profiles of the dried deposits were characterized using an optical profilometer (Bruker, Contour GT-K) and the optical microscope, as shown in Supplemental Material, Fig. S1 [39].

III. RESULTS AND DISCUSSION

A. Crack patterns under different volume fractions

The crack patterns observed for droplets dried under different volume fractions from top and side views exhibit significant variations, as illustrated in Fig. 1. It is worth noting that the crack morphologies, the number of cracks, and the shape of the deposits are strongly dependent on the initial particle volume fraction. For the smallest volume fraction used in our experiment $\phi = 0.5\%$, a ring of short straight cracks appears at the edge of the deposit, but no distinct crack pattern can be observed in the center of the droplet, as shown in Fig. 1(a). As the volume fraction is increased to $\phi = 1\%$, the area with no distinct crack pattern in the center gradually decreases in Fig. 1(b). Radial cracks form in an outer ring and eventually branch at a certain distance from the droplet edge into a multitude of secondary cracks that propagate towards the center. When the volume fraction is increased to 5%, the cracks propagate to cover nearly the entire area initially wetted by the droplet with few branching, as illustrated in Fig. 1(c). As the volume fraction further increases to $\varphi = 10\%$, the cracks uniformly expand to cover the entire deposit area, as shown in Fig. 1(d).

Remarkably, with a further increase in volume fraction of $\phi = 15\%$, fewer circular cracks occur in the deposit fragments separated by neighboring radial cracks, while the number of radial cracks formed during the drying of suspension droplet decreases in Fig. 1(e). Similar circular cracks form when drying a series of silica suspensions with volume fractions ranging from 15 to 30%, as depicted in Figs. 1(f)–1(h). Notably, a critical volume fraction of $\phi_c = 10\%$ emerges as a threshold, dividing the crack morphology into two distinct categories. Below the critical volume fraction, only radial cracks are observed on the surface, while both radial and circular cracks coexist above the critical volume fractions. Additionally, the side-view images of the deposits demonstrate significant differences for different volume fractions. The deposit fragments separated by radial cracks are warped, and the deposit looks like a spherical crown when $\phi < 10\%$. Conversely, the deposit fragments have almost no warping when $\phi > 10\%$. The volume fraction-dependent crack patterns can be better understood through a thickness dependence.

B. Thickness dependence of morphologies and crack characteristics in deposits

The drying process of the droplets and the resulting deposit morphologies can be visualized by plotting the profile of the thickness under different volume fractions of the silica colloid, as shown in Fig. 2(a). In general, two distinct deposit morphologies can be observed. At lower volume fractions, the coffee-ring effect is more pronounced [40], while at higher volume fractions, mountainlike deposit occurs. The deposit morphology is attributed to the flow of nanoparticles during evaporation. The radial flow tends to form coffee-ring deposits, with the magnitude of the effect depending on the ratio of evaporation volume flux to droplet density. On the other hand, Marangoni recirculating flow, driven by surface-tension gradient, leads to the formation of a mountainlike deposit. The transition between these deposit patterns can be explained

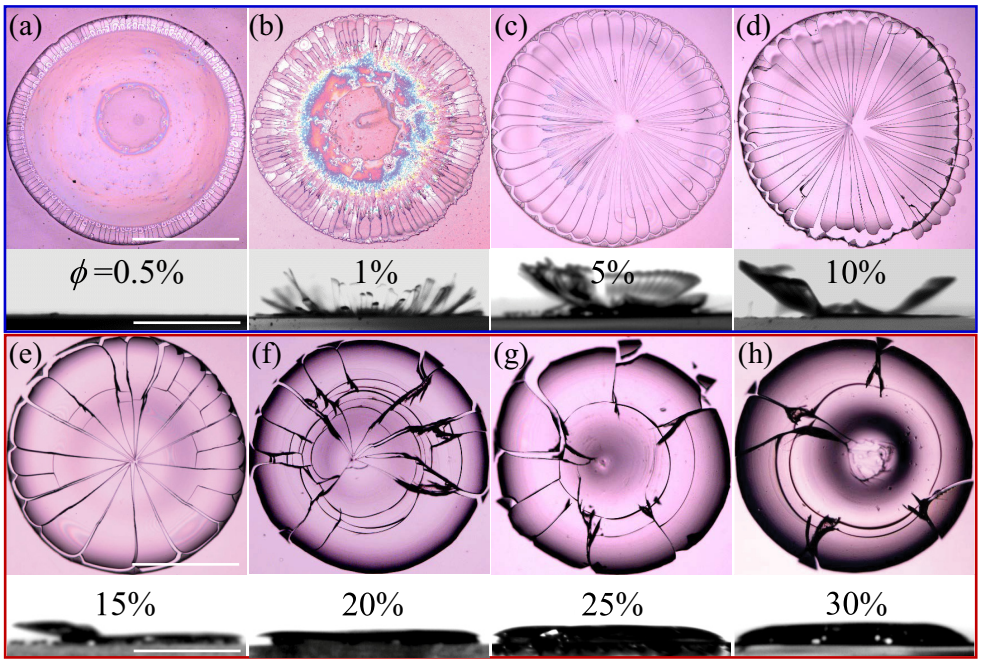

FIG. 1. Optical microscopy images of silica colloid droplets dropped on glass substrates with different volume fractions in the final dry state. The upper row represents the top view, and the lower row represents the side view. The blue box (upper) shows the radial crack morphology, while the red box (below) shows the coexistence of radial and circular cracks. (Scale bar: 1 mm.)

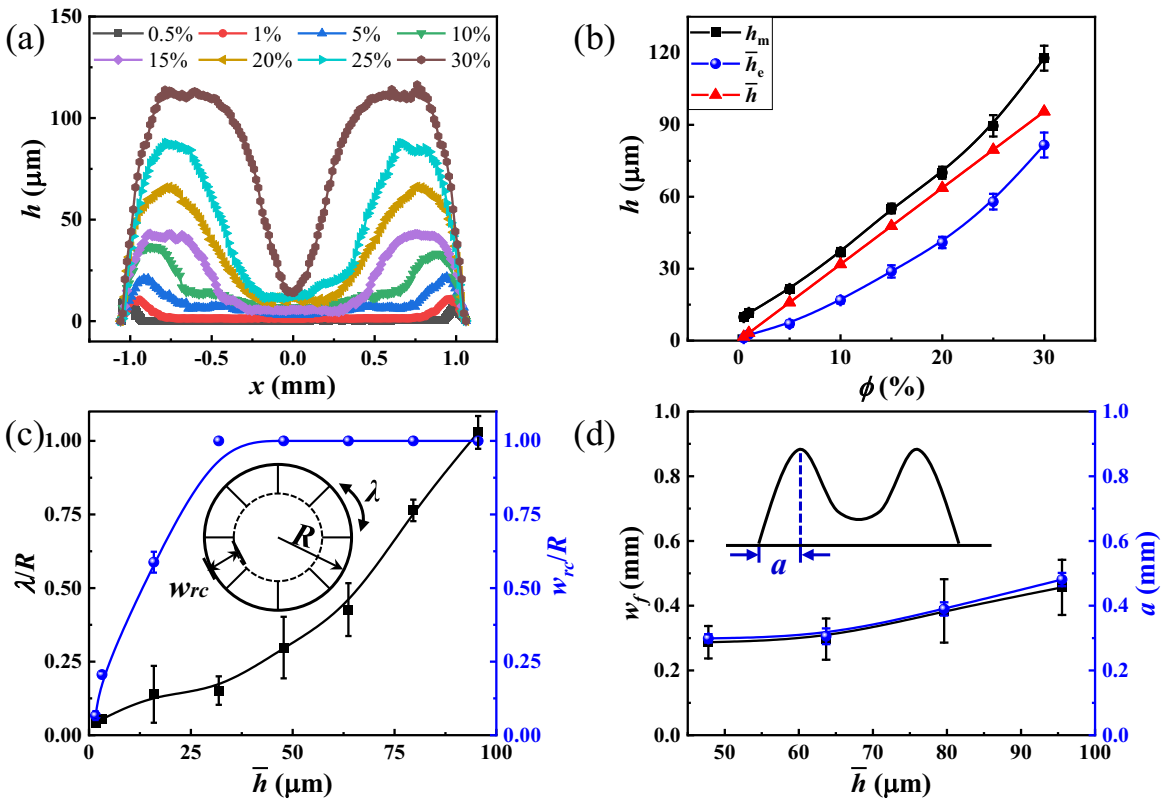

FIG. 2. (a) Thickness profiles of the dried deposits at different volume fractions. The centers of the deposits are located at $x = 0$. (b) Dependencies of the estimated average thickness $\overline{h}$ (red triangle), the experimental average thickness $\overline{h}_e$ (blue circle), and the maximum thickness h_m (black square) of the deposits on the volume fraction ϕ. (c) Plots of normalized radial crack spacing λ/R (black square) and crack propagation length w_{rc}/R (blue circle) vs $\overline{h}$. (d) Plots of the horizontal length between the edge and the maximum thickness of the deposit a (blue circle) and the length from the deposit edge to the first circular crack w_f (black square) vs the theoretical average thickness $\overline{h}$.

based on the fluid-flow model and the theoretical prediction of the deposit distribution of droplet contact-line motion [41]. In addition to deposit morphology, the volume fraction also directly affects the deposit thickness, which is a key parameter of the drying deposit. The average thickness of the deposit can be roughly estimated by $\overline{h} = \phi V/\pi R^2$. Figure 2(b) plots the estimated average thickness $\overline{h}$, the experimental average thickness $\overline{h}_e$, and the maximum thickness h_m versus initial volume fraction ϕ, respectively. It can be seen that $\overline{h}$, $\overline{h}_e$, and h_m all increase monotonically with increasing ϕ. Considering the residual liquid in the tube wall of micropipette during experimental operation and the substrate residual deposit in the measurement of deposit thickness, it is reasonable that $\overline{h}$ is slightly larger than $\overline{h}_e$. Therefore, the volume fraction-dependent crack patterns are discussed through a thickness dependence.

For quantitative analysis of these different regimes of particle deposit, we define several parameters: the droplet wetting radius R, the crack spacing λ, and the length of radial crack w_{rc}, as shown in the inset of Fig. 2(c). It is noteworthy that the radial array of cracks demonstrates exceptional periodicity and regularity, with both the crack spacing and length exhibiting a monotonic increase in relation to the theoretical average thickness of the deposit. This phenomenon can be ascribed to the wavelength of concentration fluctuation during the phase separation [42]. As the thickness increases when $\overline{h} < 31.9\,\mu$m, there is a continuous rise in the normalized crack spacing λ/R, as well as the normalized crack length w/R. Further theoretical analysis to explain the monotone variation can be found in Sec. IV B. At the critical point $\overline{h}_c = 31.9\,\mu$m, w/R reaches 1, which indicates that the radial cracks have propagated to the entire deposit surface. The discontinuous increase in crack length w_{rc} serves as a distinctive indication of the transition from coffee-ring to mountain deposits. We have measured the distance from the deposit's edge to the first circular crack, denoted as w_f. Additionally, we defined the horizontal length between the edge and the maximum thickness of the deposit as a. It can be observed that the location of the first circular crack nucleation corresponds to the location where the deposit thickness is the largest, as shown in Fig. 2(d).

To determine the stability and identify the critical average thickness for circular crack formation in silica colloidal suspension, we conducted the experiment using 20 samples for each average thickness and counted the percentage of samples exhibiting circular cracks, as shown in Supplemental Material Fig. S2(a) [39]. It is evident that the critical average thickness is approximately 31.9 μm, corresponding to around half of the samples exhibiting circular cracks. Above this thickness, both radial cracks and circular cracks coexist in the dried deposit. As the average thickness $\overline{h}$ increases, the number of circular cracks, N, initially increases and then decreases, as depicted in Supplemental Material Fig. S2(b).

In conclusion, we propose that the thickness of the deposit plays a role in regulating the crack morphology in the radial and coexisting circular and radial crack patterns promoted by delamination in silica colloidal suspension. In our experiment, we controlled the deposit thickness by adjusting the volume, volume fraction, and deposit area of the drop-coated colloidal suspension. Since the average deposit thickness is obtained by the formula $\overline{h} = \phi V/\pi R^2$, the relationship between R and ϕV is obtained by $R = \pi^{(-1/2)}\overline{h}^{(-1/2)}\sqrt{\phi V}$. A phase diagram

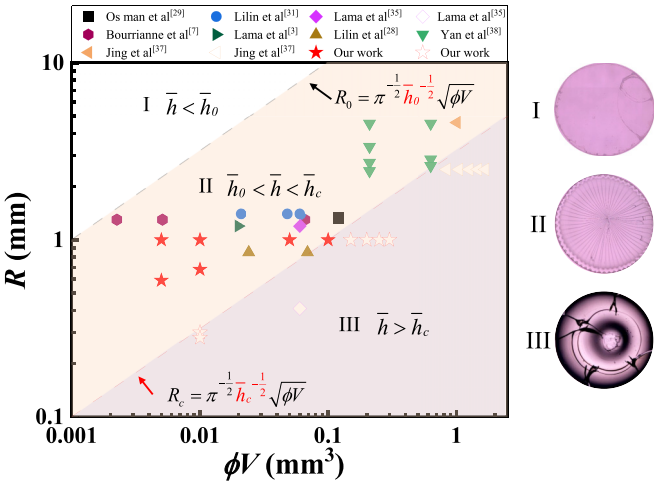

FIG. 3. Experimental observations of crack patterns in silica deposits including data from literature in the plane: (I) no crack, (II) radial crack, and (III) coexistence of radial and circular cracks. The two dashed lines are based on two estimated critical values of the average deposition thickness, where the black line (upper) is the boundary of whether a crack occurs, and the red line (below) is the boundary of whether a delamination-promoted circular crack occurs. The blank region I is the crack-free area. The orange region II is the situation of the deposit thickness below the critical thickness, while the purple region III is above the critical thickness.

for the crack morphology was constructed with respect to the deposit radius R and the volume of the deposit ϕV. Based on thickness measurements, $\overline{h_0} \approx 0.318$ μm. Based on critical value of the concentration parameters $\phi_c = 10\%$ estimated from our experiment, we obtained critical values of the average deposit thickness $\overline{h}_c = \phi_c V/\pi R^2 = 31.9\,\mu$m. $\overline{h}_0$ is the critical thickness below which films will not crack [10], and $\overline{h}_c$ is the critical thickness above which a circular crack will initiate. The two boundaries corresponding to the $\overline{h}_0$ and $\overline{h}_c$ are plotted in Fig. 3 as dashed lines in black (upper) and red (below), respectively. In addition, we extended these data extracted from relevant literature and performed additional experiment data using elastic polydimethylsiloxane (PDMS) substrates. The detailed experimental observations of colloidal deposits on the elastic PDMS substrates are shown in Supplemental Material Fig. S3 [39]. As a striking result, we observe that the crack morphologies can be accurately sorted based on the critical average deposit thickness in silica colloidal suspension. The orange region II above the dotted line, which indicates that the deposit thickness is less than the critical value, corresponds to the radial crack pattern. The purple region III below the dotted line indicates that the deposit thickness is greater than the critical value, which corresponds to the crack morphology of the coexisted radial and circular crack. These crack patterns in silica colloidal suspension have been widely observed under different parameters, such as different silica suspensions concentrations, and substrate materials. What are the underlying mechanisms that drive the transformation of the crack morphology? To address the questions, two distinct types of dynamic crack propagation were investigated separately.

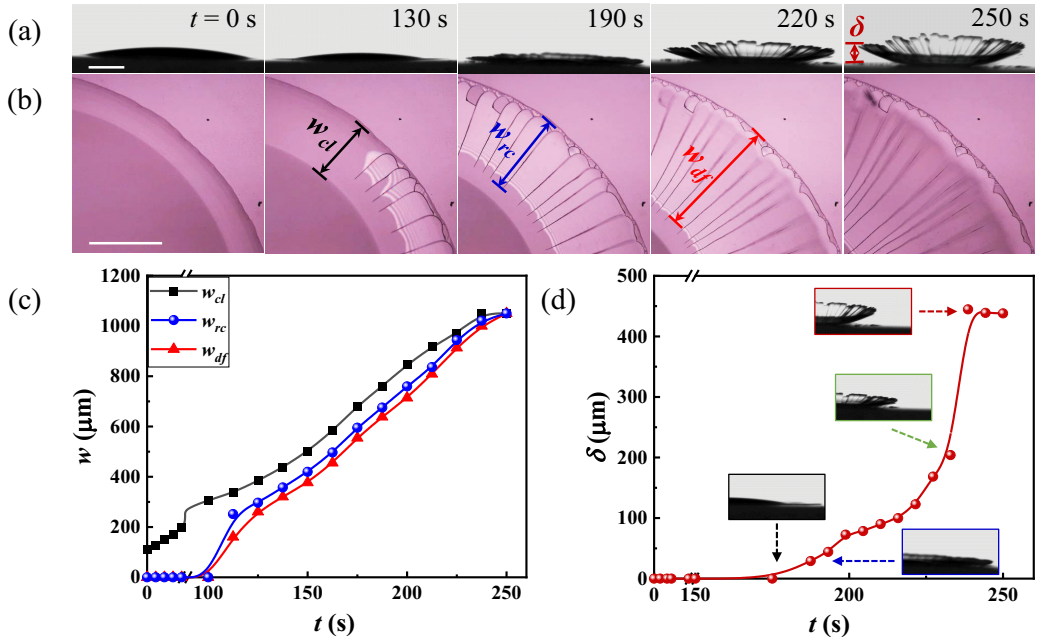

FIG. 4. *In situ* evolution of a drying colloidal droplet with $\phi = 10\%$. (a), (b) Side view and top view of formation and evolution of radial cracks. (c) Evolutions of the lengths from the deposit edge to the compaction line front w_{cl} (black square), radial crack tip w_{rc} (blue circle), and delamination front w_{df} (red triangle) with time. (d) Evolution of the deposit warping height δ with time. The insets show the side views at different time points. (Scale bar: 0.5 mm.)

C. Dynamic process of warping and cracking in deposits

To visualize the formation of radial cracks, we imaged a 1 μL suspension droplet with the volume fraction $\phi = 10\%$ on the glass slide. Upon the deposit of the silica suspensions onto the glass substrate, the liquid layer begins to evaporate immediately, causing the shrinkage of the spherical cap and the aggregation of particles. Throughout this process, the initial contact line remains pinned. In Fig. 4(a), the timestamp $t = 0$ s marks the point at which the silica suspensions solidify and transform into an obvious gel zone. The apparent compaction line gradually recedes on the deposit, resulting in the formation of a gel area that extends from the edge of the droplet towards its center [Fig. 4(b)]. Once the gel deposit reaches a certain width, and corresponds to the critical capillary pressure [40,43], the short straight cracks nucleate, accompanied by delamination. This is rapidly followed by a series of regularly spaced radial cracks along the deposit edge at $t = 130$ s. The interference fringes observed in the deposit pieces between neighboring radial cracks indicate the simultaneous occurrence of interfacial delamination during crack propagation. At $t = 190$ s, the radial cracks occupy the entire circumference of the droplet and then propagate towards the center successively with further evaporation from edge to center. Simultaneously, the delaminated deposits warp with continuous evaporation in thickness direction, which is demonstrated by the side view. Subsequently, the cracks continue to expand across the entire deposit area and delaminated deposits continue to warp, resulting in a spherical crownlike appearance in the side view. It can be seen from Fig. 4(c) that the lengths from the deposit edge to the compaction line front (w_{cl}), radial crack tip (w_{rc}), and delamination front (w_{df}) increase steadily with time until the completion of the propagation process. The warping height of the deposit (δ) also increases steadily at first, and eventually reaches a stable value, as shown in Fig. 4(d). When the liquid cap is completely evaporated, the crack reaches the center of the deposit, and fan-shaped deposit fragments are formed (Supplemental Material Movies S1 and S2).

These crack patterns are different from "daisy" cracks shown in previous study when the film-substrate adhesion is strong [30]. In this case, radial cracks form at the edge of the deposit and become disordered gradually as they move toward the center. Conversely, ordered radial cracks form and propagate from edge to center of the deposit as presented when the adhesion is relatively weak in this work. The reasons for the formation of radial cracks at the deposit edge are consistent in both cases, that is, the edge of the deposit is subject to greater hoop-tensile stress, which leads to the formation of radial cracks. The difference is that the deposit may delaminate due to weak adhesion. The occurrence of interface delamination causes the crack tip to always be subjected to greater hoop-tensile stress, which leads to continuous extending along the radial direction. A more detailed phase-field fracture model analysis can be found in Sec. IV A.

The dynamic propagation process of coexisting radial and circular cracks is shown in Fig. 5. A relatively narrow gel zone forms as the solvent evaporates [$t = 0$ s in Fig. 5(a)]. When the width of the gel zone reaches a certain threshold, radial cracks begin to form [$t = 280$ s in Fig. 5(b)]. At the same time, the dried deposit detaches from the substrate as the contact line of the droplet continuously retracts. The difference from Fig. 4(b) is that circular-shaped cracks become visible on the bottom of the deposit as it continues to warp ($t = 403$ s). At the following moment ($t = 404$ s), the deposit collapses

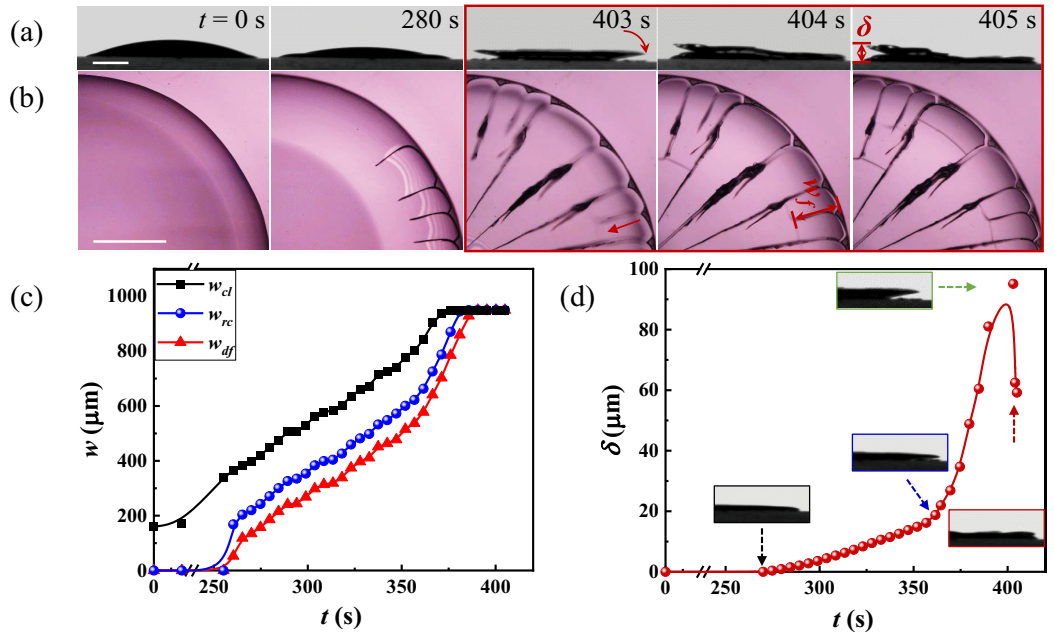

FIG. 5. *In situ* evolution of a drying colloidal droplet with $\phi = 15\%$. (a,b) Side view and top view of formation and evolution of coexisting radial and circular cracks. (c) Evolutions of the lengths from the deposit edge to the compaction line length w_{cl} (black square), radial crack tip w_{rc} (blue circle), and delamination front w_{df} (red triangle) with time. (d) Evolution of the deposit warping height δ with time. The insets show the side views at different time points. (Scale bar: 0.5 mm.)

and the circular-shaped cracks propagate through the deposit thickness (Supplemental Material Movies S3 and S4). Subsequently, more circular cracks are generated ($t = 405$ s). In Fig. 5(c), the lengths from deposit edge to the compaction line front w_{cl}, radial crack tip w_{rc}, and delamination front w_{df} extend uniformly until the crack propagation is completed, which is consistent with the case of radial cracks in Fig. 4. The difference in the generation of circular cracks is depicted in Fig. 5(d), where the insets represent the crack morphologies at different stages of crack propagation. The presence or absence of circular microcracks during warping determines the formation of the circular cracks. This unique propagation kinetics is quite different from the previously reported process of circular crack formation. Previous researchers have reported two main types of circular cracks. One type is the formation of internal precipitate ring decided by internal microstagnation flow and precipitation dynamics [33,37]. The other one is attributed to the drying-induced in-plane radial stresses generated in the colloidal deposits by varying the underlying substrate's elasticity [35]. Therefore, based on the experimental data, we propose that the circumferential strain caused by the warping of the strip deposit leads to the nucleation and growth of circular cracks in the thick deposits above the critical thickness. A more detailed theoretical analysis can be found in Sec. IV C. Therefore, the essential role of deposit thickness in determining crack morphology is attributed to the interfacial delamination that occurs during crack propagation.

Figure 6 shows a schematic of the drying process of silica colloidal droplets with two different crack morphologies. When a silica colloidal suspension is dropped onto a clean glass slide, the droplet with a spherical cap is generated, as showed in Fig. 6(a). As the solvent molecules evaporate, the droplet is dried, which usually takes about 10 min. During this process, the volume of the droplet decreases while the concentration of particles in the droplet increases, causing the spherical cap to shrink from the edge. As a result, the silica nanoparticles deposit onto the glass substrate, and form

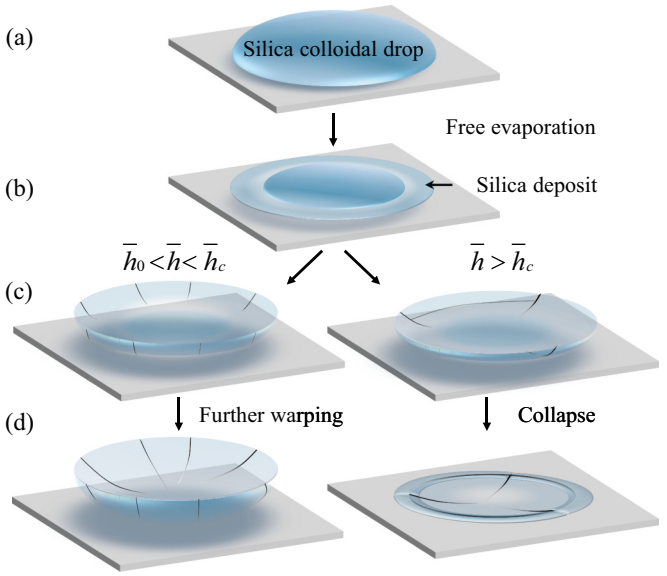

FIG. 6. Schematic illustration of the drying of colloidal droplets. (a) A droplet with a spherical cap shape adheres to a glass slide. (b) The droplet is dried to form a silica deposit from its edge through solvent evaporation. (c) Warping and cracking occur in the dried deposit, where the warped deposit will only undergo the radial cracking when $\bar{h}_0 < \bar{h} < \bar{h}_c$, while coexisting radial and circular cracks only when $\bar{h} > \bar{h}_c$. (d) Warped and collapsed deposits when the droplets with different deposit thickness are completely dried.

a silica gel deposit, as illustrated in Fig. 6(b). Both interface delamination and radial cracks occur when the tensile stress of the deposit reaches a critical value. The number of radial cracks depends on the average thickness of deposit. Simultaneously, the solvent continues to evaporate from the edge to the center and along the thickness of the deposit. On the one hand, it causes the crack tip to expand. On the other hand, it causes the deposit to warp.

When the average thickness of deposit is below the critical value ($\bar{h}_0 < \bar{h} < \bar{h}_c$), only radial cracks appear in the deposit. The radial cracks propagate from the edge toward the center of the droplet, resulting in the formation of warped deposit with radial crack patterns, as shown in Figs. 6(c) and 6(d). When the average thickness exceeds the critical value ($\bar{h} > \bar{h}_c$), not only radial cracks but also circular cracks occur. The presence of these circular cracks, together with the radial cracks, causes the deposit to collapse instead of warping further. As the deposit thickness increases, a transition from a warped deposit with radial cracks to a collapsed deposit with coexisting radial and circular cracks occurs due to the appearance of microcracks on the bottom of the deposit. Understanding the mechanisms of evolution and transition can provide insights into the design and fabrication of crack-based microstructures.

IV. THEORETICAL ANALYSIS

A. Phase-field model for radial crack formation promoted by delamination

In our study, we apply the phase-field method, a sophisticated computational approach, to elucidate the intricate relationship between delamination and crack evolution in the film-substrate system. This method, as detailed in prior research [44], can capture complex fracture patterns. It transitions from the traditional sharp, discontinuous crack model to a continuous model, utilizing a scalar damage variable, denoted as "d". This variable is designed to quantify the integrity of the material, with its value ranging from zero, which signifies an entirely unbroken region, to 1, indicating a state where the material is completely fractured. In this context, the film in our film-substrate system is conceptualized as a Föppl–von Kármán plate, characterized by a thickness h and subjected to an eigenstrain $\varepsilon^*_{\alpha\beta}$. To describe the semi-infinite elastic substrate, we employ Green's function method, and the interface between the film and substrate is effectively modeled using a cohesive zone model.

The energy present in the thin film comprises two main components: fracture energy $U^{\mathrm{f}}_{\mathrm{film}}$ and elastic energy $U^{\mathrm{el}}_{\mathrm{film}}$. Fracture energy fundamentally depends on two key factors: the critical energy release ratio G_c and the crack surface density per unit volume within the material $\gamma(d, \nabla d)$. The formula for calculating the fracture energy in the thin film is provided as [45]

$$\begin{aligned} U^{\mathrm{f}}_{\mathrm{film}} &= \int_{-h/2}^{h/2}\int_{-\infty}^{\infty}\int_{-\infty}^{\infty} G_c\gamma(\mathrm{d}, \nabla d)dx_1dx_2dx_3 \\ &= \int_{-h/2}^{h/2}\int_{-\infty}^{\infty}\int_{-\infty}^{\infty} \frac{G_c}{c_0 l_0}\left[w(d) + l_0^2\|\nabla d\|^2\right]dx_1dx_2dx_3, \end{aligned} \tag{1}$$

where l_0 is a length scale that characterizes the width of cracks, $c_0 = 4\int_0^1 \sqrt{w(s)}ds$, and $w(d)$ is the local fracture energy function, which is associated with the fracture energy. Due to the presence of cracks, the elastic modulus of the film can be expressed as follows: $C_{\alpha\beta\delta\gamma}(\mathbf{r}) = C^0_{\alpha\beta\delta\gamma}g(d, \mathbf{r})$. In this expression, $g(d, \mathbf{r})$ symbolizes a generalized degradation function, which is dependent on the evolution of cracks. For the sake of simplicity, in the subsequent discussion $g(d)$ will be used to represent this degradation function. Furthermore, $C^0_{\alpha\beta\delta\gamma}$ signifies the original elastic modulus in the absence of any cracks. Thus, the total elastic strain energy within the film is quantified by the following equation:

$$U^{\mathrm{el}}_{\mathrm{film}} = \int_{-h/2}^{h/2}\int_{-\infty}^{\infty}\int_{-\infty}^{\infty} \frac{1}{2}g(d)C^0_{\alpha\beta\delta\gamma}\varepsilon^{\mathrm{el}}_{\delta\gamma}\varepsilon^{\mathrm{el}}_{\alpha\beta}dx_1dx_2dx_3, \tag{2}$$

where $\varepsilon^{\mathrm{el}}_{\alpha\beta} = \varepsilon_{\alpha\beta} - \varepsilon^*_{\alpha\beta}$ and $\varepsilon_{\alpha\beta} = (u_{\alpha,\beta} + u_{\beta,\alpha})/2$ denote the elastic and total strains in the film, respectively. $\varepsilon^*_{\alpha\beta}$ represents the eigenstrain, which arises due to residual stresses or thermal mismatches between the film and its substrate. u_α is the middle-plane displacement of the film. Consequently, the total energy within the film comprises both fracture energy and strain energy:

$$U_{\mathrm{film}} = U^{\mathrm{f}}_{\mathrm{film}} + U^{\mathrm{el}}_{\mathrm{film}}. \tag{3}$$

In the context of the semi-infinite substrate, it interacts with the film, resulting in surface tractions. The elastic strain energy of the substrate is quantifiable as a surface integral [46]:

$$U_{\mathrm{sub}} = \frac{1}{2}\int_{-\infty}^{\infty}\int_{-\infty}^{\infty} T^{\mathrm{s}}_\alpha u^{\mathrm{s}}_\alpha dx_1dx_2. \tag{4}$$

In our analysis, T^{s}_α and u^{s}_β are the traction and displacement components on the substrate surface, respectively. Utilizing Green's function method, we articulate the surface traction T^{s}_α in terms of the surface displacement u^{s}_α. For a semi-infinite elastic substrate characterized by a shear modulus μ_s and Poisson's ratio ν_s [47], the relationship is expressed as $T^{\mathrm{s}}_\alpha = \int\int \tilde{M}_{\alpha\beta}\tilde{u}^{\mathrm{s}}_\beta e^{i\xi_\alpha x_\alpha}d\xi_1d\xi_2/(2\pi)^2$. In this formulation, $\tilde{M}_{\alpha\beta}$ is Green's function within the Fourier domain, ξ_α represents its corresponding Fourier vector, and $\tilde{u}^{\mathrm{s}}_\beta$ characterizes the displacement of the substrate u^{s}_β within this domain. The wave symbol ($\tilde{}$) placed above a variable signifies its Fourier transform.

In our study, the interface between the film and substrate is elucidated using a cohesive zone model. The properties of this interface are encapsulated by a nonlinear traction-separation relation, derived from a potential-energy function [48]:

$$T_\alpha = \frac{2\Gamma_t\Lambda_\alpha}{\delta_t^2}\exp\left(-\frac{\Lambda_t^2}{\delta_t^2}\right), \tag{5}$$

where $\Lambda_t = \sqrt{\Lambda_1^2 + \Lambda_2^2}$ are the tangential components of the displacement jump across the interface, δ_t is the characteristic length of interface tangential displacement jump, and Γ_t denotes the interface strength. Consequently, the energy on the interface is given by

$$U_{\mathrm{int}} = \int_{-\infty}^{\infty}\int_{-\infty}^{\infty}\int_0^{\Lambda_\alpha} T_\alpha \mathrm{d}\Lambda_\alpha dx_1dx_2. \tag{6}$$

Therefore, the comprehensive free energy of the entire film-substrate system, including the film, substrate, and interface, is

$$U_{\text{tot}} = U_{\text{film}} + U_{\text{sub}} + U_{\text{int}}. \tag{7}$$

This system's total energy is expressible as a function of the interface displacement jump Λ_α, in-plane displacement u_α, and crack order parameter d. The process of minimizing the total free energy is governed by the time-dependent Ginzburg-Landau kinetic equations [46], enabling accurate modeling of the morphological evolution of cracks and delamination, as described by

$$\frac{\partial \Lambda_\alpha}{\partial t} = -\Gamma_{\Lambda_\alpha}\left(T_\alpha - T_\alpha^{\text{s}}\right), \tag{8}$$

$$\frac{\partial u_\alpha}{\partial t} = -\Gamma_{u_\alpha}\left\{-\left[g(d)hC_{\alpha\beta\delta\gamma}\varepsilon_{\delta\gamma}^{\text{el}}\right]_{,\beta} + T_\alpha^{\text{s}}\right\}, \tag{9}$$

$$\frac{\partial d}{\partial t} = -\Gamma_d\left\{\frac{1}{2}g(d)'hC_{\alpha\beta\delta\gamma}^0\varepsilon_{\delta\gamma}^{\text{el}}\varepsilon_{\alpha\beta}^{\text{el}} + \frac{G_c h}{c_0 l_0}\left[w(d)' - 2l_0^2\nabla^2 d\right]\right\}. \tag{10}$$

Here, Γ_{Λ_α}, Γ_{u_α}, and Γ_d are the dynamic relaxation coefficients related to the interface displacement jump Λ_α, in-plane displacement u_α, and crack order parameter d, respectively, driving the rate of evolution and reflecting the unique properties of the material system. By applying the microelasticity theory, we incorporate the equivalent intrinsic strain $\varepsilon_{\alpha\beta}^0$, and transpose the problem of heterogeneous elastic systems to a homogenized system augmented by $\varepsilon_{\alpha\beta}^0$ [49]. As a result, Eq. (8) is reformulated as

$$\frac{\partial \varepsilon_{\alpha\beta}^0}{\partial t} = -\Gamma_{\varepsilon_{\alpha\beta}^0}hC_{\alpha\beta\delta\gamma}^0\left\{-\varepsilon_{\delta\gamma} + [1-g(d)]^{-1}\left(\varepsilon_{\delta\gamma}^0 - \varepsilon_{\delta\gamma}^*\right) + \varepsilon_{\delta\gamma}^*\right\}. \tag{11}$$

To solve Eqs. (7), (9), and (10), we use the semi-implicit spectral method [50]. Therefore, the model we have established provides an approach to understanding the synergistic evolution of thickness-through crack in the film and interface delamination. Additionally, a scalar parameter $D = 1$ is introduced to characterize the delamination state when $\Lambda_t > \delta_t$.

We employed a phase-field model established herein to conduct simulation analyses to investigate the evolution of crack, delamination, and the difference between circumferential stress σ_θ and radial stress σ_r under different interface strengths, as depicted in Fig. 7. Our initial setup involved the mismatch strain $\varepsilon^* = -0.05$, the shear modulus ratio of 1 : 1 between the film and the substrate, and Poisson's ratios of the film $\nu_f = 0.3$ and substrate $\nu_s = 0.3$. We defined the ratio of dynamic evolution coefficients for fracture and delamination, $\Gamma_d/\Gamma_{\Lambda_\alpha} = 2$. In our simulations, to qualitatively demonstrate how the formation of radial cracks is facilitated by simultaneous delamination as shown in our experimental observations, we maintained the critical energy release rate $G_c/\mu_s l_m = 0.002$, where μ_s is the shear modulus of the substrate and l_m is the unit grid length; we adjusted the ratio of interface strength to the critical energy release rate $\Gamma_t/G_c = 5$ and 5×10^4, representing scenarios of low and high interface strength, respectively. These parameters are set to guarantee that there are nucleation and growth of thickness-through crack in the film with the delamination, as Γ_t is comparable to G_c, and without the delamination, as Γ_t is much larger than G_c.

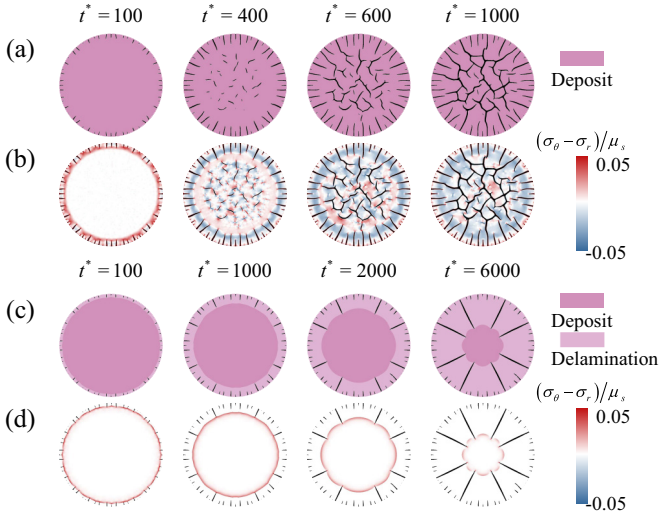

FIG. 7. Numerical simulation results of crack propagation without or with delamination. The evolution process of (a) crack pattern, and (b) the anisotropic state of stress in the thin film with strong interface strength. The evolution process of (c) crack pattern and (d) the anisotropic state of stress in the thin film with relative weak interface strength. The time t^* is normalized by $t/\mu_s l_m \Gamma_{\varepsilon_{\alpha\beta}^0}$, where μ_s is the shear modulus of the substrate, and l_m is the unit grid length. The σ_r represents the radial stress and the σ_θ represents the circumferential stress.

Our visual representations employ deep pink to denote deposit, light pink to highlight the delamination area, and black to indicate the presence of cracks. As shown in Fig. 7(a), under high interface strength conditions, delamination is absent. Cracks initially nucleate at the boundary, followed by radial propagation. Subsequently, due to the residual stresses, crack formation eventually occurs in the central region of the film. The chaotic and disordered crack development is attributed to the isotropic internal stresses within the film. Over time, a network forms as external and internal cracks intersect and interconnect. When examining the first primary stress σ_1 evolution, it is observed that initial crack formation at the boundary generates numerous stress concentration points within the film in Fig. S4(a). As these cracks evolve, the energy within the film is progressively released, leading to system stabilization. In contrast, under low interface strength conditions, delamination and crack formation occur concurrently at the boundary, as shown in Fig. 7(c). The delamination front remains aligned with the crack tip, promoting continuous radial crack propagation. The analysis of the first primary stress evolution suggests that most of the energy in the delamination area is dissipated through interface delamination, with some residual stress persisting near the delamination front due to boundary effects in Fig. S4(b). In the simulation, $(\sigma_\theta - \sigma_r)/\mu_s$ represents the anisotropic state

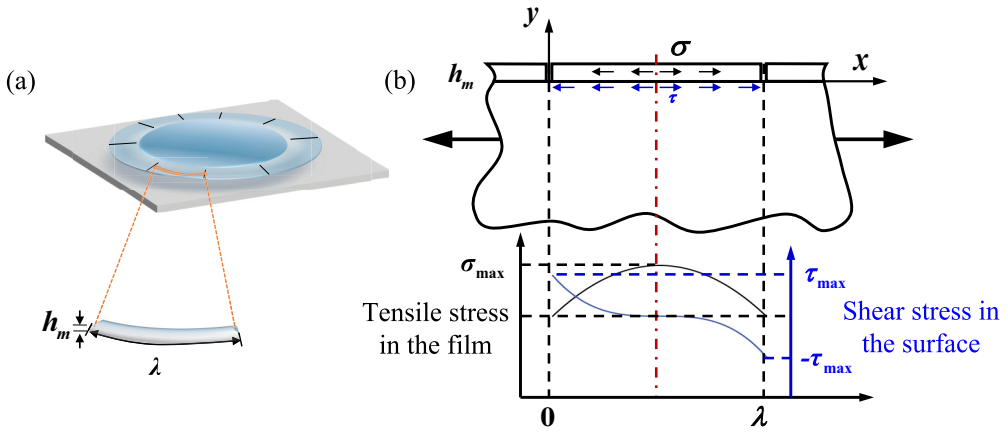

FIG. 8. (a) Schematic for a layered substrate of multiple cracks induced in the film. The symbols λ and $\bar{h}$ are the spacing between radial cracks and the thickness of the deposit, respectively. (b) A detailed two-dimensional shear lag model of stress distributions in the cracked segments of the film. The symbols σ and τ are the tensile stress and the interfacial shear stress in the film, respectively.

of stress within the thin film. As depicted in Fig. 7(b), except for the edge of the deposit that is subject to circumferential stress due to the edge effect, the rest of the area is subject to isotropic stress and produces disordered cracks. Most of the residual stress perpendicular to the direction of the crack is released by the crack; parallel to the crack, directional stresses still exist. However, the degree of stress anisotropy consistently reaches its peak near both the delamination front and the crack tip [Fig. 7(d)]. This is accompanied by the coordinated advancement of these fronts, leading to a pattern of radial crack propagation. Consequently, it can be deduced that the anisotropy of the stress field at the crack tip, induced by interface delamination, directs the radial propagation of cracks. Furthermore, due to the delamination effect, most of the stress σ_1/μ_s in the delaminated area of the film is released, as illustrated in Fig. S4(b). Consequently, there is no residual energy available to drive the formation of additional cracks. Additionally, the absence of stress concentration areas in the central region of the film prevents the initiation of new cracks. For the reasons outlined above, only radial cracks were observed in the thin film. It is noteworthy that out-of-plane warping was not considered in this analysis. This omission is reasonable because the out-of-plane displacement of the film at the front of crack propagation and delamination is very small, and its impact on crack evolution can be ignored. Consequently, the phase-field model we developed effectively elucidates the growth mechanisms of radial cracks, aligning closely with the experimental observations in Fig. 4.

B. Analysis of the relationship between crack spacing and deposit thickness

The deposits are divided into many segments with equal spacings as modeled in Fig. 8(a). The experimental pattern in Fig. 1 shows that this idealization is not very far from reality. We used a shear lag model [51,52] to analyze the relationship between the spacing of radial cracks in the deposit λ and the thickness of the deposit $\bar{h}$, as shown in Fig. 8(b). At locations far away from previously formed cracks, when the maximum tensile stress σ_m in the deposit reaches the critical value σ_c, which is a material parameter, another crack occurs. Therefore, the variation of $\tau(x)$ with x also affects the relationship between λ and $\bar{h}$. Here, we assume $\tau(x)$ to be a constant; to simplify, we can get an approximate relationship between the length of a cracked segment λ and the thickness of the film $\bar{h}$:

$$\lambda = \frac{2\sigma_c \bar{h}}{\tau}. \tag{12}$$

In fact, for different types of $\tau(x)$, crack spacing λ also maintains a positive correlation with film thickness, $\lambda \propto \bar{h}^b (b > 0)$, but except for different exponential parameters b. The specific calculation of b also needs to consider the actual interface situation.

C. Analysis of nucleation and nucleation position of circular crack

In situ observations under the microscope during the desiccation process in Fig. 5 suggest the following mechanism. Since evaporation starts from the colloidal surface, the humidity gradient in the thickness direction causes a stress-gradient distribution; stress in the porous deposit drives the accumulation of elastic strain energy, and when it overcomes the adhesion energy of the deposit attached to the substrate, delamination occurs, as shown in Fig. 9. The circular structures are formed after the radial crack and delamination propaga-

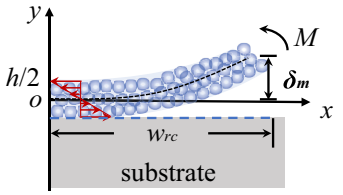

FIG. 9. Delamination schematic of a drying colloidal promoted by thickness-dependent drying in silica colloidal deposits. The stress distribution results in a moment per unit depth, M, and causes the film to warp.

tion. To elucidate the nucleation and propagation of circular crack above the critical deposit thickness h_c, we adopted the flexural cantilever model in mechanics of materials. For the striped deposit between two radial cracks, we assume it is a beam structure. The stress generated by warping in the deposit is

$$\sigma = \frac{My}{I}, \tag{13}$$

in which M is the warping moment, y is the distance from a point to the neutral layer in the thin deposit, and I is the area moment of inertia about the neutral axis. For the pure warping case, the deflection $\delta(x)$ and warping moment M have the following differential relationship:

$$\frac{d^2\delta}{dx^2} = \frac{M}{EI}, \tag{14}$$

where E is the elastic modulus of the thin deposit. Therefore, the stress in the thin deposit is

$$\sigma = yE\delta(x)''. \tag{15}$$

It is obvious that the point with the highest stress $\sigma_{\max} = \delta(x)''Eh/2$ in the deposit will inevitably appear on the bottom of the deposit, regardless of the change of δ''. When the stress at the bottom of the deposit exceeds the local material strength, circular crack is nucleated.

However, the specific location where the maximum tensile stress occurs at the bottom surface of the deposit fragment depends on the deposit thickness, and second derivative of warping deflection based on the theoretical analysis of a curved beam. For deposits with variable thicknesses, obviously the circular crack is more likely to occur at the position with the largest film thickness. Such prediction based on the qualitative is in good agreement with the experiment in Fig. 2(d).

V. CONCLUSIONS

In summary, our study reveals a remarkable change in the thickness profile and crack patterns in the colloidal deposits obtained by drying a range of different deposit thicknesses. A critical average deposit thickness of approximately 31.8 μm marks a threshold for this transition. The thickness profile transitions from a coffee ring to a mountain shape, while the crack pattern changes from radial crack to coexisting radial and circular cracks, accompanied by delamination. The synergy propagation processes of crack and delamination are shown by *in-situ* experimental observation. The formation mechanism of the radial crack is revealed by phase-field fracture model, which is the change in stress distribution at the crack tip induced by delamination. Circumferential strain at the bottom surface of the striped deposit induced by warping leads to nucleation and growth of circular cracks above critical thickness. Although cracks are usually viewed as a failure, the robust control over diverse crack morphologies induced by the collaborative mode here can turn cracks into a design tool for spontaneous substrate patterning, which may serve as a valuable tool in the design and manufacturing of micronano devices.

ACKNOWLEDGMENTS

This work was supported by the National Natural Science Foundation of China (Grants No. 12025206 and No. 12172113), the National Key Research and Development Program of China (Grant No. 2022YFA1203602), the Strategic Priority Research Program of the Chinese Academy of Sciences (Grant No. XDB0620101), and the Zhejiang Provincial Natural Science Foundation of China (Grant No. LZ23A020003). This work was partly carried out at the Experimental Center of Engineering and Material Sciences at USTC.

[1] D. J. Harris, H. Hu, J. C. Conrad, and J. A. Lewis, Phys. Rev. Lett. **98**, 148301 (2007).
[2] N. Rana and S.-T. Yau, Nanotechnology **15**, 275 (2004).
[3] H. Lama, M. Basavaraj, and D. Satapathy, Soft Matter **13**, 5445 (2017).
[4] H. Hu and R. Larson, J. Phys. Chem. B **106**, 1334 (2002).
[5] C. Allain and L. Limat, Phys. Rev. Lett. **74**, 2981 (1995).
[6] J. Hutchinson and Z. Suo, Adv. Appl. Mech. **29**, 63 (1992).
[7] P. Bourrianne, P. Lilin, G. Sintès, T. Nîrca, G. McKinley, and I. Bischofberger, Soft Matter **17**, 8832 (2021).
[8] Y. Popov, Phys. Rev. E **71**, 036313 (2005).
[9] M. Smith and J. Sharp, Langmuir **27**, 8009 (2011).
[10] K. B. Singh and M. S. Tirumkudulu, Phys. Rev. Lett. **98**, 218302 (2007).
[11] T. Ye and Z. Suo, Int. J. Solids Struct. **29**, 2639 (1992).
[12] L. Pauchard, Europhys. Lett. **74**, 188 (2006).
[13] V. Lazarus and L. Pauchard, Soft Matter **7**, 2552 (2011).
[14] R. W. Style, S. S. L. Peppin, and A. C. F. Cocks, J. Geophys. Res. Earth **116**, F01025 (2011).
[15] F. Boulogne and H. Stone, Europhys. Lett. **108**, 19001 (2014).
[16] Z. Néda, K.-t. Leung, L. Józsa, and M. Ravasz, Phys. Rev. Lett. **88**, 095502 (2002).
[17] V. X. Nguyen and K. J. Stebe, Phys. Rev. Lett. **88**, 164501 (2002).
[18] J. Xu, J. Xia, S. W. Hong, Z. Lin, F. Qiu, and Y. Yang, Phys. Rev. Lett. **96**, 066104 (2006).
[19] V. Dugyala, H. Lama, D. Satapathy, and M. Basavaraj, Sci. Rep. **6**, 30708 (2016).
[20] J. Kim, K. Cho, S. Ryu, S. Kim, and B. Weon, Sci. Rep. **5**, 13166 (2015).
[21] J. Marthelot, B. Roman, J. Bico, J. Teisseire, D. Dalmas, and F. Melo, Phys. Rev. Lett. **113**, 085502 (2014).
[22] M. Liu, S. Yu, L. He, and Y. Ni, Soft Matter **18**, 5906 (2022).
[23] L. Goehringa, L. Mahadevanb, and S. Morrisa, Proc. Natl. Acad. Sci. USA **106**, 387 (2009).
[24] X. Ma, J. Lowensohn, and J. C. Burton, Phys. Rev. E **99**, 012802 (2019).
[25] L. Pauchard, M. Adda-Bedia, C. Allain, and Y. Couder, Phys. Rev. E **67**, 027103 (2003).
[26] L. Goehring, W. Clegg, and A. Routh, Soft Matter **7**, 7984 (2011).

[27] K. Leung, L. Jòesa, M. Ravasz, and Z. Néda, Nature (London) **410**, 166 (2002).
[28] P. Lilin and I. Bischofberger, Langmuir **38**, 7442 (2022).
[29] A. Osman, L. Goehring, H. Stitt, and N. Shokri, Soft Matter **16**, 8345 (2020).
[30] M. Gao, X. Huang, and Y. Zhao, Sci. China Technol. Sci. **61**, 949 (2018).
[31] P. Lilin, P. Bourrianne, G. Sintès, and I. Bischofberger, Phys. Rev. Fluids **5**, 110511 (2020).
[32] L. Pauchard, F. Parisse, and C. Allain, Phys. Rev. E **59**, 3737 (1999).
[33] S. Maheshwari, L. Zhang, Y. Zhu, and H.-C. Chang, Phys. Rev. Lett. **100**, 044503 (2008).
[34] L. Shmuylovich, A. Shen, and H. Stone, Langmuir **18**, 3441 (2002).
[35] H. Lama, T. Gogoi, M. G. Basavaraj, L. Pauchard, and D. K. Satapathy, Phys. Rev. E **103**, 032602 (2021).
[36] C. He, Z. Xie, Z. Guo, and H. Yao, J. Mech. Phys. Solids **83**, 19 (2015).
[37] G. Jing and J. Ma, J. Phys. Chem. B **116**, 6225 (2012).
[38] N. Yan, H. Luo, H. Yu, Y. Liu, and G. Jing, Colloids Surf., A **624**, 126780 (2021).
[39] See Supplemental Material at http://link.aps.org/supplemental/10.1103/PhysRevE.110.034801 for details about the film thickness measurement, the proportion and number of circular cracks and the crack morphology of different substrates under a variety of film thickness, and *in situ* observation movie of crack propagation. Three supplemental figures and four movies are provided.
[40] R. Deegan, O. Bakajin, T. Dupont, G. Huber, S. Nagel, and T. Witten, Nature (London) **389**, 827 (1997).
[41] X. Man and M. Doi, Phys. Rev. Lett. **116**, 066101 (2016).
[42] J. Ma and G. Jing, Phys. Rev. E **86**, 061406 (2012).
[43] A. Sarkar and M. Tirumkudulu, Soft Matter **7**, 8816 (2011).
[44] A. J. Pons and A. Karma, Nature **464**, 85 (2010).
[45] T. Hu, J. Guilleminot, and J. Dolbow, Comput. Methods Appl. Mech. Eng. **368**, 113106 (2020).
[46] Y. Ni, L. He, and Q. Liu, Phys. Rev. E **84**, 051604 (2011).
[47] K. Pan, Y. Ni, L. He, and R. Huang, Int. J. Solids Struct. **51**, 3715 (2014).
[48] X. Xu and A. Needleman, J. Mech. Phys. Solids **42**, 1397 (1994).
[49] Y. U. Wang, Y. M. Jin, and A. G. Khachaturyan, Acta Mater. **52**, 81 (2004).
[50] L. Chen and J. Shen, Comput. Phys. Commun. **108**, 147 (1998).
[51] M. Yanaka, Y. Tsukahara, N. Nakaso, and N. Takeda, J. Mater. Sci. **33**, 2111 (1998).
[52] A. McGuigan, G. Briggs, V. Burlakov, M. Yanaka, and Y. Tsukahara, Thin Solid Films **424**, 219 (2003).